Applied Catalysis B: Environmental 140–141 (2013) 42–50

Contents lists available at SciVerse ScienceDirect

Applied Catalysis B: Environmental

journal homepage: www.elsevier.com/locate/apcatb

Room-temperature catalytic removal of low-concentration NO over mesoporous Fe–Mn binary oxide synthesized using a template-free approach

Zhu Shu[a], Yu Chen[a], Weimin Huang[a], Xiangzhi Cui[a], Lingxia Zhang[a], Hangrong Chen[a], Guobin Zhang[a], Xiangqian Fan[a], Yongxia Wang[a], Guiju Tao[a], Dannong He[b], Jianlin Shi[a,*]

[a] State Key Laboratory of High Performance Ceramics and Superfine Microstructure, Shanghai Institute of Ceramics, Chinese Academy of Sciences, 1295 Dingxi Road, Shanghai 200050, PR China
[b] National Engineering Research Center for Nanotechnology, 28 East Jiangchuan Road, Shanghai 200241, PR China

ARTICLE INFO

Article history:
Received 6 December 2012
Received in revised form 4 March 2013
Accepted 20 March 2013
Available online 26 March 2013

Keywords:
Mesoporous Fe–Mn binary oxide
Low-concentration NO
Catalytic oxidation
Adsorption
Room temperature

ABSTRACT

A novel template-free approach, the controlled thermal decomposition of single-phase Fe–Mn binary oxalate, was proposed and used to synthesize mesoporous Fe–Mn binary oxide, which possessed homogeneous worm-like mesopores (4–5 nm) and high surface areas above 200 m^2/g. The catalyst was efficient in the catalytic removal of low-concentration NO at room temperature: 100% removal of 10 ppm NO in the first 4 h at a high space velocity of 40,000 h^{-1} on a Fe–Mn binary oxide with a Fe/Mn ratio of 1/4 calcined at 300 °C. Catalysts with other Fe/Mn ratios or calcined at higher temperatures showed lower NO removal performances. A synergetic effect between Mn^{n+} and Fe^{n+} was proposed and believed to be responsible for the catalytic conversion of NO and O_2 into NO_2, which was subsequently adsorbed and/or absorbed as nitrates on the binary oxide.

© 2013 Elsevier B.V. All rights reserved.

1. Introduction

In cities, the number of mobile vehicles are increasing quickly. In order to facilitate the transportation and parking, more and more road tunnels and indoor parks have been constructed. However, these semi-closed spaces have low ventilation efficiencies and thus retain the car exhausts therein, causing serious localized air pollution. For instance, tens ppm of NO_x (generally 90% NO and others NO_2) have been normally detected, which are harmful to the drivers and passengers [1–3]. Forced ventilation is not only highly energy-consuming but can also lead to air pollution in the surroundings. Therefore, relevant in situ remediation technologies are urgently demanded and begin to attract increasing attention.

Selective catalytic reduction (SCR) [4] and NO_x storage/reduction (NSR) [5], i.e. turning NO_x into N_2, are the most developed techniques for NO_x removal. However, their high working temperatures (generally above 200 °C) hinder the application in the removal of NO_x at room temperature in road tunnels and indoor parks. Thus, novel room-temperature de-NO_x approaches are in great need of development. A promising alternation is to adsorb or absorb NO_x at room temperature and separate it from the air. Previous studies show that NO is much harder to be adsorbed or absorbed than NO_2 due to its super-low normal boiling point (−152 °C) and inert chemical activities [6–8]. Therefore, a highly efficient catalytic sorbent is necessary which should be able to effectively catalyze the oxidation of NO into NO_2 at room temperature before NO_2 adsorption or absorption in order to achieve a high NO_x removal efficiency.

However, such a type of catalytic sorbent has not been well explored. The most-studied materials able to catalyze the oxidation of NO at room temperature are microporous materials, such as actived carbon fibers [9–11] and zeolites [12,13]. Unfortunately, their catalysis efficiencies will dramatically decrease at the decreased initial NO concentration down to about one hundred of ppm, indicating that they are competent only for the oxidation of concentrated NO of hundreds or more ppm (the case in fuel exhaust gases) but not for the oxidation of low-concentration NO of tens or less ppm (the case in road tunnels and indoor parks) [10]. Moreover, these microporous materials are not efficient in the adsorption or absorption of NO_2, meaning an additional subsequent NO_2 adsorption and/or absorption is indispensable. The only reported materials showing both room-temperature NO oxidation and adsorption/absorption functions are Fe–Mn based transition metal oxides prepared by the traditional co-precipitation method [14]. Unfortunately, only the NO removal at relatively high

* Corresponding author at: 1295 Dingxi Road, Shanghai 200050, PR China. Tel.: +86 21 52412712; fax: +86 21 52413122.
E-mail address: jlshi@sunm.shcnc.ac.cn (J. Shi).

0926-3373/$ – see front matter © 2013 Elsevier B.V. All rights reserved.
http://dx.doi.org/10.1016/j.apcatb.2013.03.030

concentration (400 ppm) was examined, and the removal of NO at as low as tens ppm remained an un-solved issue. In addition, the specific surface area of as-prepared Fe–Mn mixed oxide was not high enough (54 m^2/g) [14], which might exhibit unsatisfactory catalytic activity.

Mesoporous material is well-known for high specific surface areas and well structured mesopores (2–50 nm in diameters), which leads to enhanced performances in many applications such as catalysis, adsorption and separation [15–20]. Various mesoporous transition metal oxides have been synthesized in the past decade [21–26]. However, to the best of our knowledge, there is no report on mesoporous Fe–Mn binary oxide yet. The dominated method for synthesizing mesoporous metal oxide is the replication route using mesoporous silica as a hard template, which is multi-step and time-consuming [27–30]. Hence, increasing attempts have been made to develop facile template-free routes. Our groups have proposed a facile template-free strategy to prepare mesoporous metal oxides such as Mn_2O_3, NiO, and Fe_2O_3 with high surface areas and well-controlled pore structure by a controlled thermal decomposition of their metal oxalates [31,32].

Herein, we apply this template-free strategy to synthesize mesoporous Fe–Mn binary oxide with high surface area from single-phase Fe–Mn binary oxalate, and use it for the removal of low-concentration NO (10 ppm) at room temperature. The characteristics of Fe–Mn oxide were tuned by changing the Fe/Mn ratio and calcination temperature, and the NO removal performances of Fe–Mn oxides were investigated. Finally, the effect of the characteristics of the Fe–Mn oxide on its NO removal performance and corresponding mechanisms of the NO catalytic removal were discussed.

2. Experimental

2.1. Material preparation

All the chemicals used were of analytical grade, purchased from Sinopharm Chemical Reagent Co. Ltd. and used without further purification. The novel mesoporous Fe–Mn binary oxide was template-freely synthesized by calcining a precursor of Fe–Mn binary oxalate, which was precipitated from a Fe^{2+}–Mn^{2+} solution mixed with oxalic acid. In a typical experiment, a mixture of $FeSO_4{\cdot}7H_2O$ and $MnCl_2{\cdot}4H_2O$ (0.06 mol in total) was dissolved in 80 mL deionized water by magnetic stirring in air. Meanwhile, 0.06 mol of $C_2H_2O_4{\cdot}2H_2O$ was dissolved in 30 mL deionized water at 60 °C. Then, the latter solution was added dropwise into the former under vigorous magnetic stirring, during which a yellow precipitate formed. Then, the resultant precipitate was stirred for another 1 h in an ice bath, filtered, washed with deionized water and ethanol, and dried at 70 °C in air overnight. The as-obtained yellow powder precursor was calcined in air at 300 °C (or other aim temperatures) for 1 h using a heating rate of 1 °C/min. The ratio of $FeSO_4{\cdot}7H_2O$ to $MnCl_2{\cdot}4H_2O$ was varied to synthesize samples with different Fe/Mn molar ratios of 1/8, 1/4 and 1/2. The precursors and calcined samples were labeled as Fe_xMn_y-oxalate and Fe_xMn_y-*z* respectively, where *x*/*y* stood for the Fe/Mn molar ratio in the parent solution and *z* represented the calcination temperature. In addition, the precursors and relevant calcined samples purely with Mn (or Fe) were also prepared as contrasts, which were labeled as Mn (or Fe)-oxalate and Mn (or Fe)-*z*, respectively.

2.2. NO removal test

The NO removal tests were performed in a quartz tubular fixed-bed flow reactor with an inner diameter of 8 mm, using 0.1 g of sample. The reaction temperature was controlled at 25 °C by a thermostatic waterbath. The typical reactant gas composition was 10 ppm NO (similar to the level in the air of road tunnels and indoor parks), 21% O_2, and balance N_2. The total flow rate was 200 mL/min under ambient conditions and the GHSV (gas hourly space velocity) was calculated to be 40,000 h^{-1}. To investigate the effect of H_2O on the NO removal process, the balance N_2 was humidified by passing through a bottle of deionized water and a relative humidity of 88% was achieved in the reactant gas. In each test, the sample was pretreated in flowing N_2 at 150 °C for 2 h and cooled to the reaction temperature, and then N_2 was switched to the reactant gas. The NO and NO_2 concentrations in the inlet and outlet gas were online monitored by the NO_x analyzer (Thermo Fisher 42i-LS). The NO removal ratio was calculated using Eq. (1), in which NO_{inlet} and NO_{outlet} stood for the NO concentrations in the inlet and outlet gases respectively.

$$\text{NO removal ratio}\,(\%) = \frac{NO_{inlet} - NO_{outlet}}{NO_{inlet}} \times 100 \quad (1)$$

Temperature programmed desorption (TPD) of the sample after NO removal test was carried out by heating the used sample to 300 °C with a heating rate of 1 °C/min in N_2, using a flow rate of 200 mL/min. The desorbed NO and NO_2 concentrations were online detected by the NO_x analyzer.

2.3. Characterization

X-ray powder diffraction (XRD) patterns were recorded on a Rigaku D/Max 2200PC diffractometer using Cu Kα radiation at 40 kV and 40 mA. Thermogravimetric/differential thermal analyzer (TG-DTA) measurements were conducted using a NETZSCH STA 449C apparatus with an air flow of 20 mL/min and a heating rate of 10 K/min. Nitrogen adsorption/desorption isotherms at 77 K were measured on a Micromeritics TriStar 3020 porosimeter. All samples were outgassed at 150 °C for 6 h under flowing nitrogen before measurements. The specific surface areas were calculated with the Brunauer–Emmet–Teller (BET) methods. Pore volume and pore size distribution plots were obtained by Barrett–Joyner–Halenda (BJH) method using the cylindrical pore model. Field emission scanning electron microscopy (SEM) analysis was performed on a JEOL JSM6700F electron microscope. Field emission transmission electron microscopy (TEM) analysis was conducted on a JEOL 200CX electron microscope operated at 200 KV. Fourier transform infrared (FTIR) spectra were recorded with a Nicolet iS10 FTIR spectrometer. X-ray photoelectron spectroscopy (XPS) signals were collected on a Thermo Scientific ESCALAB 250 instrument using monochromated Al X-ray resource at 1486.6 eV operated at 15 kW. All the elemental binding energies were referenced to the C (1s) line situated at 285 eV.

3. Results and discussion

3.1. Characteristics of the precursors

Fig. 1A presents the XRD patterns of the precursors with different Fe/Mn ratios and that of the precursor purely with Mn (or Fe). All the precursors are well crystallized. First attention should be paid to those of Mn-oxalate (Fig. 1A-a) and Fe-oxalate (Fig. 1A-e), which can be indexed to $MnC_2O_4{\cdot}2H_2O$ (JCPDS 25-0544) and $FeC_2O_4{\cdot}2H_2O$ (JCPDS 22-0635), respectively. Fe_xMn_y-oxalates generally show XRD patterns similar to those of Mn-oxalate and Fe-oxalate with slight difference. The Fe_1/Mn_8-oxalate pattern (Fig. 1A-b) resembles Mn-oxalate (Fig. 1A-a) most, and those of Fe_xMn_y-oxalates become more distinguishable from Mn-oxalate at the increased Fe/Mn ratio (from Fig. 1A-b to Fig. 1A-d), which however get more similar to that of Fe-oxalate (Fig. 1A-e). Moreover, it can be seen that each Fe_xMn_y-oxalate pattern contains identical

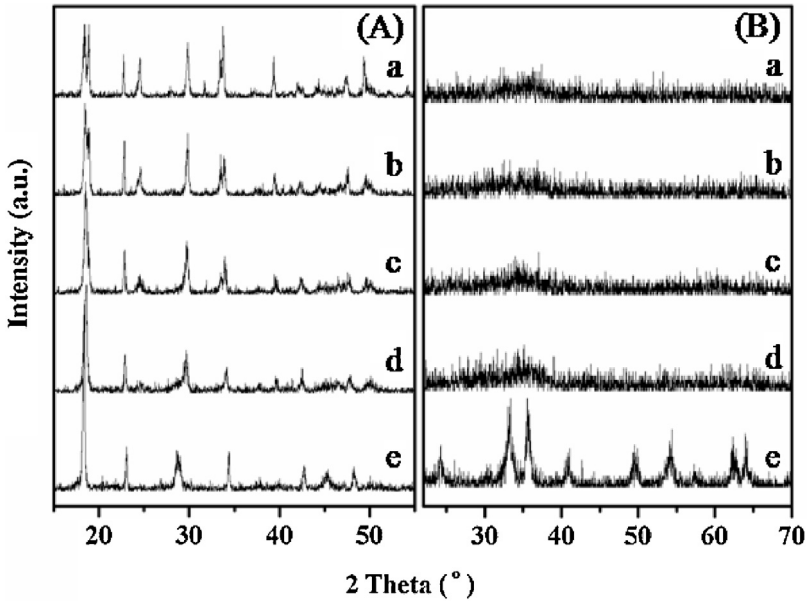

Fig. 1. XRD patterns of (A) the oxalate precursors and (B) 300 °C calcined counterparts of (a) Mn-sample, (b) Fe_1Mn_8-sample, (c) Fe_1Mn_4-sample, (d) Fe_1Mn_2-sample and (e) Fe-sample.

or fewer peaks than those of either Mn-oxalate or Fe-oxalate. If Fe_xMn_y-oxalate was a simple mixture of two single-metal oxalates, its XRD pattern would contain more peaks than either Mn-oxalate or Fe-oxalate. Therefore, Fe_xMn_y-oxalate can be identified as a single-phase binary oxalate and its chemical formula could be rewritten as $Fe_{x/(x+y)}Mn_{y/(x+y)}C_2O_4{\cdot}2H_2O$.

The TG and DTA curves of Mn-oxalate, Fe-oxalate, and Fe_1Mn_4-oxalate (representing the Fe_xMn_y-oxalates) are shown in Fig. 2. Each oxalate shows one endothermic peak and one exothermic peak. The endothermic peaks at 143, 213 and 173 °C for Mn-oxalate, Fe-oxalate and Fe_1Mn_4-oxalate, respectively, correspond to the losses of structural water (weight losses of about 20%), and meanwhile the exothermic peaks at 346, 276 and 318 °C for Mn-oxalate, Fe-oxalate and Fe_1Mn_4-oxalate, respectively, represent the decompositions of the oxalate groups (weight losses of approximately 35%). The fact that, Fe_1Mn_4-oxalate shows new endothermic and exothermic peaks differing from those of either Mn-oxalate or Fe-oxalate, demonstrates that the former is a new single phase but not a mixture of the latter two.

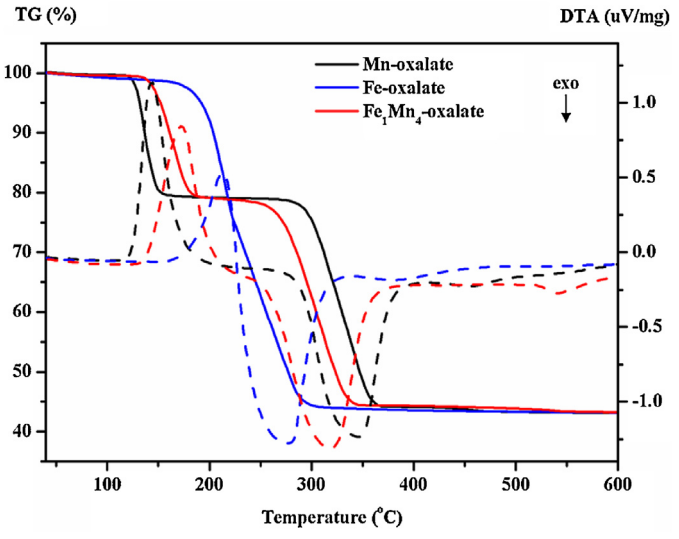

Fig. 2. TG and DTA curves of Mn-oxalate, Fe-oxalate and Fe_1Mn_4-oxalate.

Fig. 3 exhibits the SEM morphologies of Mn-oxalate, Fe-oxalate, and Fe_1Mn_4-oxalate. The three kinds of metal oxalates clearly show different morphologies. Mn-oxalate and Fe-oxalate particles are big lamellar boards (Fig. 3a) and irregular cuboids (Fig. 3b), respectively, whereas Fe_1Mn_4-oxalate (Fig. 3c) has a more uniform morphology of cubes, which visually proves again Fe_xMn_y-oxalate to be new single-phase.

Herein, it can be summarized that single-phase Fe–Mn binary oxalate can be easily obtained by precipitation from a Fe^{2+}–Mn^{2+} solution mixed with oxalic acid.

3.2. Characteristics of the calcined samples

The XRD patterns of samples calcined at 300 °C are also shown in Fig. 1. Only Fe-300 (Fig. 1B-e) is crystallized, corresponding to α-Fe_2O_3 (JCPDS 33-0664), and the other samples Mn-300 (Fig. 1B-a) and Fe_xMn_y-300 (Fig. 1B-b, c and d) are amorphous to XRD. This result indicates that Fe_xMn_y-300 is not a mixture of Fe-300 and Mn-300 but a new Fe–Mn binary oxide of single phase, which accords with the above result that the precursor Fe_xMn_y-oxalate is single-phase. Calcination at elevated temperatures results in the crystallization of Fe–Mn oxide, as can be seen in Fig. S1. Other than the amorphous Fe_1Mn_4-300 (Fig. 1B-c), Fe_1Mn_4-400 (Fig. S1a) has a XRD pattern featured with diffraction peaks indexed to α-Mn_2O_3, indicating its preliminary crystallization, and the formation of crystallized α-Mn_2O_3 (JCPDS 65-7467) is detected in Fe_1Mn_4-500 (Fig. S1b).

The SEM morphologies of Mn-300, Fe-300 and Fe_1Mn_4-300 are also shown in Fig. 3. Comparing the calcined samples (Figs. 3d, e and f) with the corresponding precursors (Figs. 3a, b and c), it can be seen that, after calcination, each type of samples has generally retained its original morphology but with substantial cracks. Moreover, limited size shrinkage can be found, in spite of the high total weight loss up to about 55%, as estimated from the TG curves in Fig. 2. Thus, significant porosity can be inferred within the calcined samples, which are demonstrated by the TEM observations in Fig. 4. It can be seen that homogeneous worm-like mesopores are randomly distributed within the whole sample. During calcination,

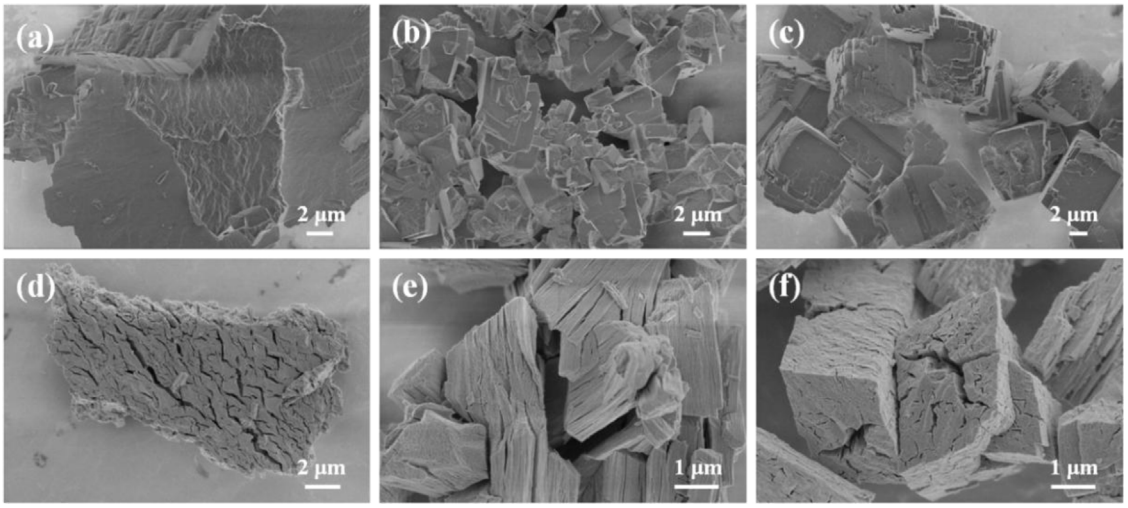

Fig. 3. SEM morphologies of the oxalate precursors: (a) Mn-oxalate, (b) Fe-oxalate, and (c) Fe_1Mn_4-oxalate, and those of the calcined counterparts: (d) Mn-300, (e) Fe-300, and (f) Fe_1Mn_4-300.

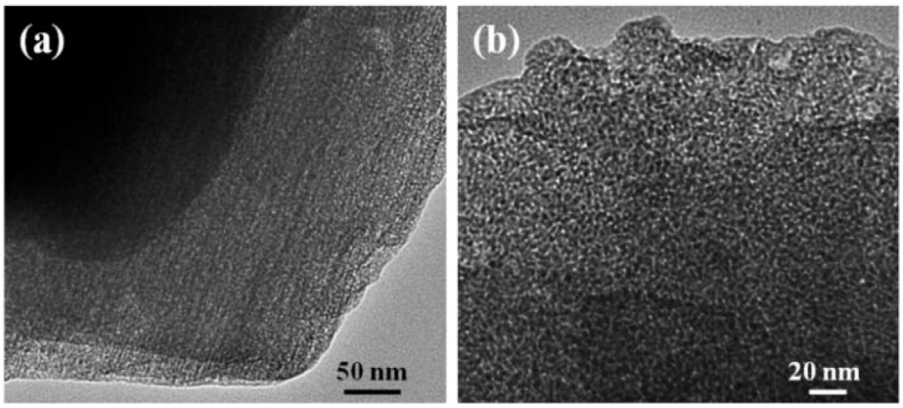

Fig. 4. (a) TEM image of Fe_1Mn_4-300 and (b) magnified TEM image to show its well-defined mesoporous structure.

the $C_2O_4^{2-}$ anions and structural water decomposed and released gaseous CO_2 and H_2O, leaving behind numerous voids, and then pores were formed by the packing among adjacent primary metal oxide particles of several nanometers. Other calcined samples have similar TEM morphologies which are not shown here.

N_2 adsorption–desorption isotherms and the BJH desorption pore size distribution plots of Mn-300, Fe_xMn_y-300 and Fe-300 are shown in Fig. 5, and the pore structure parameters are summarized in Table 1. All the samples have typical Langmuir IV curves with hysteresis loops, which prove their mesoporous structure. The pore size distribution curves suggest that all the samples have defined mesoporosities. The pore size at the maximum probability of the Fe–Mn binary oxide decreased from 4.9, 4.4 to 4.3 nm for Fe_1Mn_8-300, Fe_1Mn_4-300 and Fe_1Mn_2-300 of increased Fe/Mn ratio, respectively. For the single-metal oxides, Mn-300 exhibits a relatively boarder pore size distribution and has two kinds of pore sizes at the maximum probabilities (4.3 and 7.0 nm), and Fe-300 has

Table 1
Pore structural parameters of samples Mn-300, Fe_1Mn_8-300, Fe_1Mn_4-300, Fe_1Mn_4-400, Fe_1Mn_4-500, Fe_1Mn_2-300 and Fe-300.

Sample	Calcination temperature (°C)	BET surface area (m^2/g)	d_{BJH} (nm)	Pore volume (cm^3/g)
Mn-300	300	149	7.0	0.30
Fe_1Mn_8-300	300	218	4.9	0.33
Fe_1Mn_4-300	300	240	4.4	0.34
Fe_1Mn_4-400	400	231	5.0	0.43
Fe_1Mn_4-500	500	28	28.1	0.26
Fe_1Mn_2-300	300	253	4.3	0.37
Fe-300	300	95	8.2	0.30

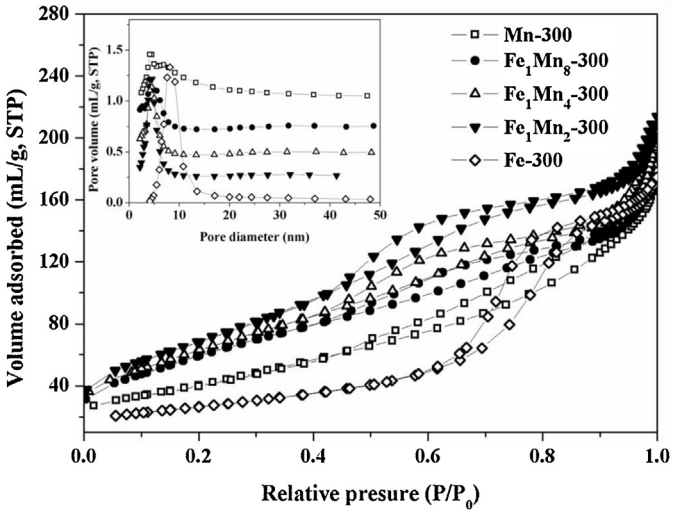

Fig. 5. N_2 adsorption–desorption isotherms and BJH desorption pore size distribution plots (insert) of the samples calcined at 300 °C.

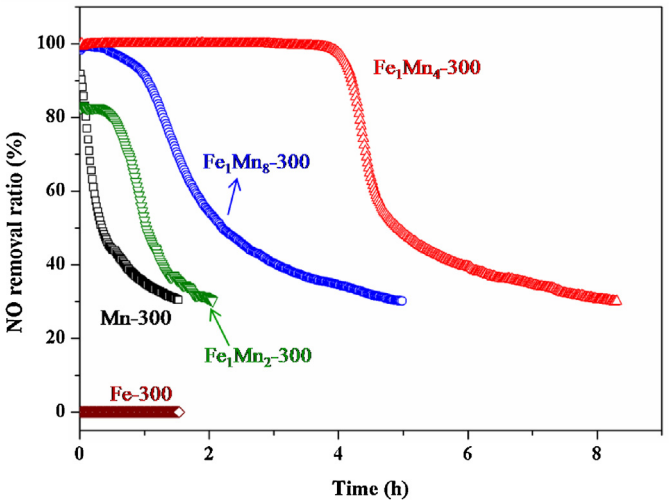

Fig. 6. Time courses of NO removal on Mn-300, Fe_1Mn_8-300, Fe_1Mn_4-300, Fe_1Mn_2-300 and Fe-300. Reaction conditions: [NO] = 10 ppm, [O_2] = 21%, balance = N_2, temperature = 25 °C and GHSV = 40,000 h^{-1}.

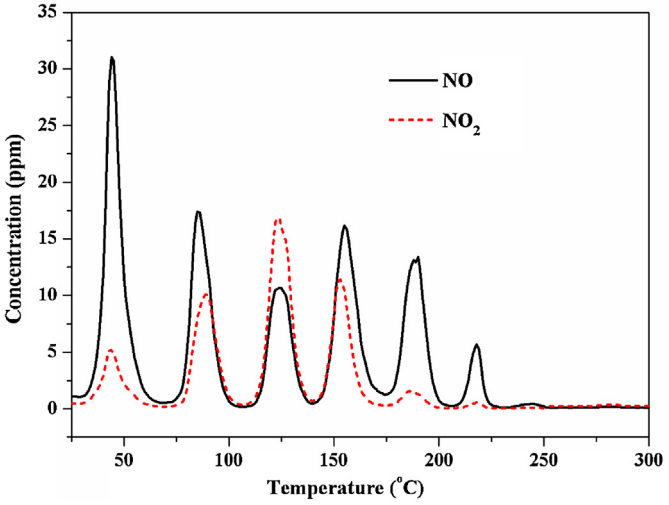

Fig. 7. TPD curve of Fe_1Mn_4-300 after the NO removal test for 12 h.

the biggest pore size at the maximum probability (8.2 nm). Moreover, the specific surface area and pore volume of the Fe–Mn binary oxides increased as the Fe/Mn ratio increased from Fe_1Mn_8-300 (218 m^2/g and 0.33 cm^3/g), Fe_1Mn_4-300 (240 m^2/g and 0.34 cm^3/g) to Fe_1Mn_2-300 (253 m^2/g and 0.37 cm^3/g), while those of single-metal oxides were much lower such as Mn-300 (149 m^2/g and 0.30 cm^3/g) and Fe-300 (95 m^2/g and 0.30 cm^3/g). The higher specific surface areas can be attributed to smaller pore sizes and higher pore volumes. The porosity differences demonstrate again that the Fe–Mn binary oxide calcined at 300 °C (Fe_xMn_y-300) is a new single phase but not a simple mixture of Fe-300 and Mn-300.

Fe_1Mn_4-samples calcined at elevated temperatures (400 and 500 °C) still have well-defined mesoporous structure, demonstrated by the N_2 adsorption–desorption isotherms and BJH desorption pore size distribution plots (Fig. S2) and the pore structural parameters which are detailed in Table 1. However, with the increase of calcination temperature, smaller pores would be eliminated by Oswald ripening, while bigger pores grew even bigger. The pore size at the maximum probability increased from 4.4 nm (for Fe_1Mn_4-300) to 5.0 and 28.1 nm for Fe_1Mn_4-400 and Fe_1Mn_4-500, respectively, and the BET surface area decreased accordingly due to Oswald ripening.

3.3. Application in NO removal at room temperature

Fig. 6 shows the NO removal performances of the samples calcined at 300 °C. Fe-300 is not capable of NO removal at all. The NO removal ratio of Mn-300 was 90% at the beginning, but decreased immediately and dramatically down to 50% in as short as 0.4 h. However, the Fe–Mn binary oxides show much higher NO removal efficiencies than that of either Mn-300 or Fe-300, which indicates the presence of a synergetic effect between Mn and Fe elements within the binary oxides. In detail, with the lowest Fe/Mn ratio, Fe_1Mn_8-300 removed almost 100% of NO in the first 0.5 h, and then the NO removal percentage decreased gradually to 50% in 2.3 h. As the Fe/Mn ratio increases to 1/4, the Fe_1Mn_4-300 shows enhanced NO removal efficiency, 100% of NO could be continuously converted for as long as 4 h, and then the conversion reduced to 50% in 5 h. However, further increased Fe/Mn ratio leads to degraded performance: Fe_1Mn_2-300 removed 84% of NO at first, and then decreased to 50% in 1.1 h.

Calcination at elevated temperatures leads to lower NO removal efficiency of the Fe–Mn oxide, as observed by comparing the NO removal performances of Fe_1Mn_4-400 and Fe_1Mn_4-500 (Fig. S3) with that of Fe_1Mn_4-300 (Fig. 6). Considering the porosity (Table 1) and lattice structure (Fig. 1B and Fig. S1) differences, the decrease of NO removal efficiency can be ascribed to the decrease of specific surface area and the crystallization of iron manganate. Smaller specific surface area signifies lower amounts of active sites, and the crystallization may lead to activity loss of these sites. Moreover, since Fe_1Mn_4-400 possesses a BET surface area (231 m^2/g) highly comparable to that of Fe_1Mn_4-300 (240 m^2/g) but shows much worse performance in NO removal, it can be inferred that the NO removal efficiency is primarily affected by the phase structure (crystallization), and an amorphous phase is believed to be crucial for a high NO removal efficiency.

The TPD curve of Fe_1Mn_4-300 after the NO removal test for 12 h is shown in Fig. 7. It can be seen that a large amount of NO and NO_2 was desorbed during the temperature elevating, which ended at around 250 °C. About six distinguished desorption peaks can be observed, which should be corresponding to six different existing states of NO_x as adsorbed molecules, nitrites and/or nitrates on/in the Fe–Mn binary oxide, and the peak at elevated temperature corresponds to stronger adsorption or more stable existence of nitrogen-containing compounds. The regenerated Fe_1Mn_4-300 after the TPD test was used for NO removal again, and the results are plotted in Fig. S4. It shows that, when Fe_1Mn_4-300 was regenerated and reused once, it exhibited a favorable NO removal performance comparable to that of the fresh Fe_1Mn_4-300 with a slight loss of NO removal capacity. When Fe_1Mn_4-300 was regenerated and reused twice or three times, its NO removal capacity can also be recovered mostly but with increased capacity losses, as indicated by the gradual decrease in the 100% NO removal time durations. The gradual decrease in the NO removal capacity can be attributed to the loss of the active catalytic sites due to reasons such as the un-sufficient desorption of formed nitrogen-containing compounds. The above results demonstrate the preferable reusability of the synthesized Fe_1Mn_4-300 catalyst for NO removal.

To clarify the NO removing process on the Fe–Mn binary oxide, the time courses of outlet NO and NO_2 concentrations in the NO removal test on Fe_1Mn_4-300 is detailed in Fig. 8. Three stages can be identified in the NO removal process. In the stage-I, no NO_x can be found in the outlet gas, indicating a complete adsorption and/or absorption (corresponding to NO_x storage of 0.16 mmol/g counted by integral calculus). In the stage-II, NO_2 breaks through

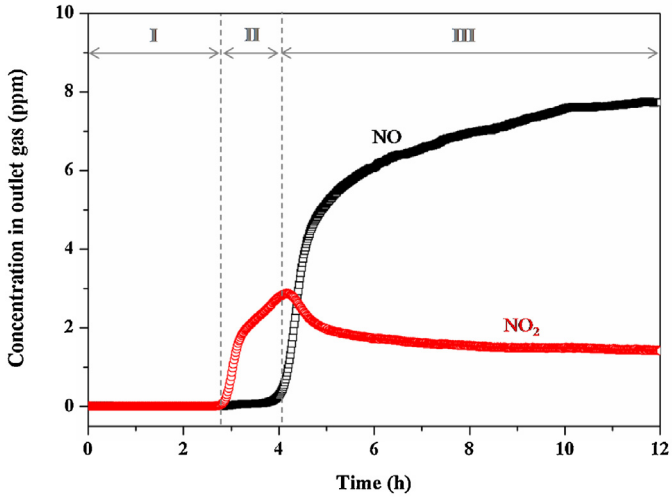

Fig. 8. Time courses of outlet NO and NO_2 concentrations during the NO removal test on Fe_1Mn_4-300. Reaction conditions: [NO] = 10 ppm, [O_2] = 21%, balance = N_2, temperature = 25 °C and GHSV = 40,000 h^{-1}.

with increasing concentrations (corresponding to NO_x storage of 0.051 mmol/g and NO_2 release of 0.013 mmol/g). In the stage-III, NO breaks through and its concentration increases while that of NO_2 decreases (corresponding to NO_x storage of 0.077 mmol/g and NO_2 release of 0.078 mmol/g). The FTIR spectra (Fig. 9) of Fe_1Mn_4-300 before and after the NO removal test for 12 h demonstrate that, nitrate species as proved by the band 1384 cm^{-1} have formed on the Fe–Mn oxide, meanwhile, weakly adsorbed NO_2 proved by the band 1630 cm^{-1} can also be found. Previously, Huang and Yang [14] demonstrated the formation of nitrites and its transformation into nitrates on Fe–Mn mixed oxides in the NO adsorption process, benefiting from the use of in situ FTIR technique. Therefore, a possible NO removal process can be proposed as follows. On the Fe–Mn binary oxide, NO is catalytically oxidized to NO_2 in the presence of O_2, and NO_2 is further adsorbed and reacts with the metal oxides to form nitrites and finally nitrates. Hence, NO_x is totally removed at the beginning (stage-I). In the time course, the formed nitrites and nitrates cover/occupy the increasing numbers of active sites of Fe–Mn oxide so that not all formed NO_2 can be adsorbed, leading to the breakthrough of NO_2 into the outlet gas (stage-II). Further coverage of active sites of the bimetal oxide by the nitrites

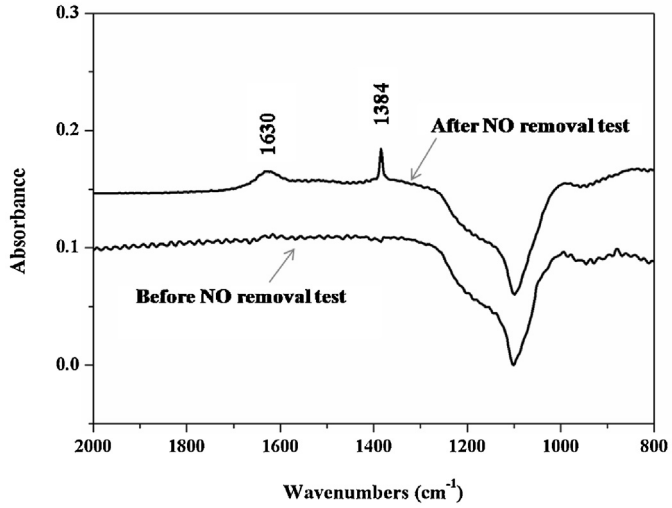

Fig. 9. FTIR spectra of Fe_1Mn_4-300 before and after the NO removal test.

and nitrates significantly prevented inlet NO from being oxidized to NO_2, and thus the NO break-through takes place in about 4 h of reaction, and quickly increasing amount of NO pass through the Fe–Mn oxide in the following course, resulting in the increased NO and in the meantime decreased NO_2 concentrations in the outlet gas (stage-III).

XPS analysis (Fig. 10), mainly on Mn 2p and Fe 2p, was conducted on Fe_1Mn_4-300 before and after the NO removal test, which aims to detect its surface chemical states and reveal the mechanism of NO catalytic oxidation on the Fe–Mn binary oxide. There are two peaks observed for Mn $2p_{3/2}$ (642.4 eV) and Mn $2p_{1/2}$ (654.0 eV) (Fig. 10A), and two peaks for Fe $2p_{3/2}$ (711.3 eV) and Fe $2p_{1/2}$ (725.2 eV) (Fig. 10B). Peak fitting is carried out for Mn $2p_{3/2}$ and Fe $2p_{3/2}$, and the distribution of metal ions is detailed in Table 2. For both the fresh and used Fe_1Mn_4-300, the Mn $2p_{3/2}$ spectra can be separated into three characteristic peaks at about 641 eV, 642 eV and 644 eV, corresponding to Mn^{2+}, Mn^{3+} and Mn^{4+}, respectively [33,34]. Meanwhile, Mn^{3+} and Mn^{4+} account for the vast majority (about 95% together) and Mn^{2+} is very few (Table 2). For the Fe $2p_{3/2}$ spectra, two characteristic peaks can be separated by peak fitting at about 710 eV and 712 eV corresponding to Fe^{2+} and Fe^{3+}, respectively [34–36]. It is noted that, after the NO removal test, there is a variation on the valence states of Mn^{n+} and Fe^{n+}, i.e., the amounts of Mn^{4+} and Fe^{2+} increased while those of Mn^{3+} and Fe^{3+} decreased accordingly. This phenomenon implies the occurrence of an electronic transfer process between Mn^{n+} (mainly Mn^{4+} and Mn^{3+}) and Fe^{n+} (Fe^{3+} and Fe^{2+}) in the NO removal, which is further applied to propose a synergetic effect on the catalytic oxidation of NO to NO_2 in the presence of O_2 through two possible routes as illustrated in Scheme 1. In the proposed route-1 (Scheme 1a), Mn^{4+} gains an electron from Fe^{2+}, and they become Mn^{3+} and Fe^{3+}. Then Fe^{3+} adsorbs the NO molecule and captures one electron from it, in the meantime Fe^{3+} changes back to Fe^{2+} and NO is activated into NO^+ species. Meanwhile, Mn^{3+} adsorbs an O_2 molecule and donates an electron to the O atom, in the meantime Mn^{3+} becomes Mn^{4+} and O_2 is activated into O^- species. Finally, the reaction between activated NO^+ and O^- species leads to the quick formation of NO_2. In contrast in the proposed route-2 (Scheme 1b), Fe^{3+} gains an electron from Mn^{3+}, and they become Fe^{2+} and Mn^{4+}. Then similar NO and O_2 activation processes by Mn^{4+} and Fe^{2+}, respectively, take place, leading to the NO oxidation. Previously, Chen et al. [34] observed similar valence state variation of Mn^{n+} and Fe^{n+} in low temperature (80–220 °C) SCR of NO using Fe–Mn mixed oxide containing $Fe_3Mn_3O_8$ phase, and they proposed a NO oxidation route similar to Scheme 1b. We believe that both two routes might contribute to the catalytic oxidation of NO, and the route of Scheme 1a might be more dominant so that the relative amounts of Mn^{4+} and Fe^{2+} increased after the NO removal test (Table 2). Additionally, since the proposed synergetic effect functions through the valence variation of Mn^{n+} and Fe^{n+} in the Fe–Mn oxide, an amorphous framework of the Fe–Mn oxide is considered to be more preferable which may favors the changes of the metal ion valences. This accords with the above inference by comparing the Fe–Mn oxides' NO removal performances and their crystallization degrees, that is, an amorphous phase is believed to be favorable for a high NO removal efficiency.

In addition, H_2O was found to be harmful in the NO removal process on Fe–Mn oxide. As plotted in Fig. S5, a relative humidity of 88% significantly reduced the NO removal performance of Fe_1Mn_4-300, which can be attributed to the competitive occupancy of NO_x adsorption/absorption sites by water molecules. In view of the fact that the air in the road tunnels and indoor parks are usually humid, a pre-drying process of the inlet air will be necessary when using Fe–Mn oxides for in situ NO_x remediation. Besides, CO_2 and SO_2 in the practical air may also compete with NO_x in the adsorption/absorption process, which however has not been evaluated in this study yet.

Table 2
XPS of Mn 2p and Fe 2p in Fe_1Mn_4-300 before and after the NO removal test.

		Before NO removal test		After NO removal test	
	Phase	Binding energy (eV)	Percentage (%)	Binding energy (eV)	Percentage (%)
Mn	Mn^{2+}	641.2	5.6	641.2	4.4
2p	Mn^{3+}	642.2	64.1	642.2	57.3
	Mn^{4+}	644.5	30.3	644.2	38.3
Fe	Fe^{2+}	710.5	34.8	710.5	40.4
2p	Fe^{3+}	712.1	65.2	711.9	59.6

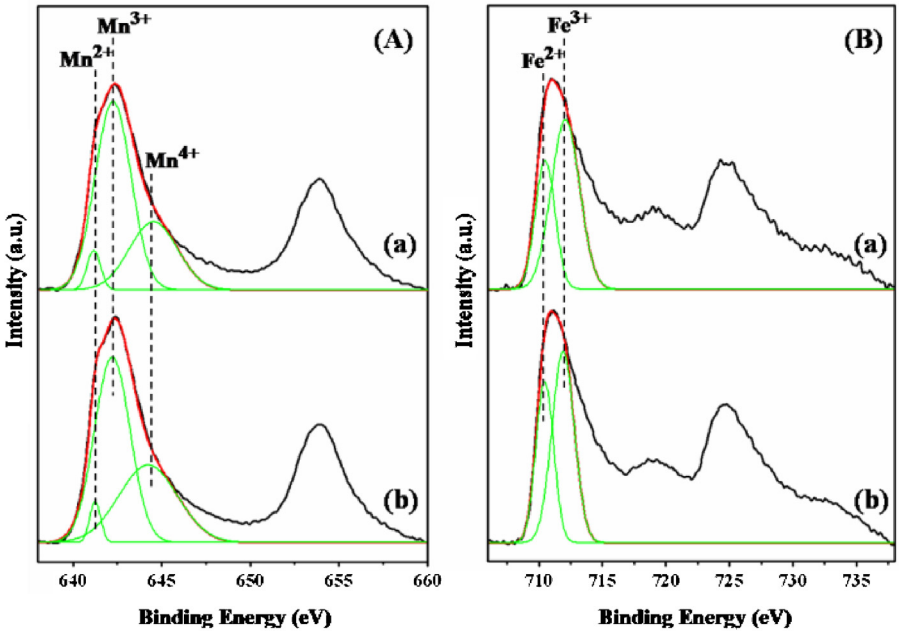

Fig. 10. XPS spectra of (A) Mn 2p and (B) Fe 2p in Fe_1Mn_4-300 (a) before and (b) after the NO removal test.

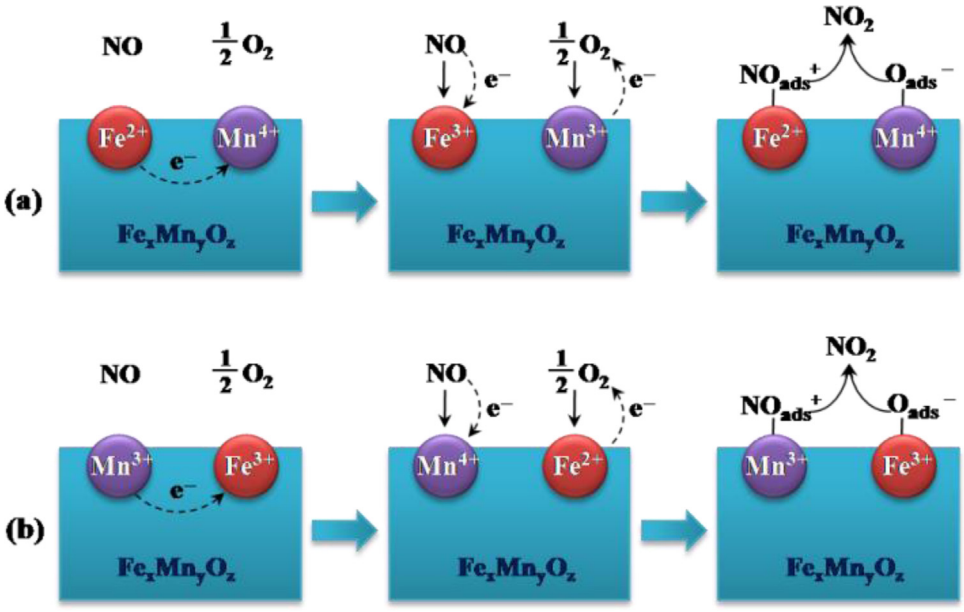

Scheme 1. The proposed synergetic catalytic effects between Mn^{n+} and Fe^{n+} in Fe–Mn binary oxide by two possible ways responsible for the activation of NO and O_2 and their conversion to NO_2.

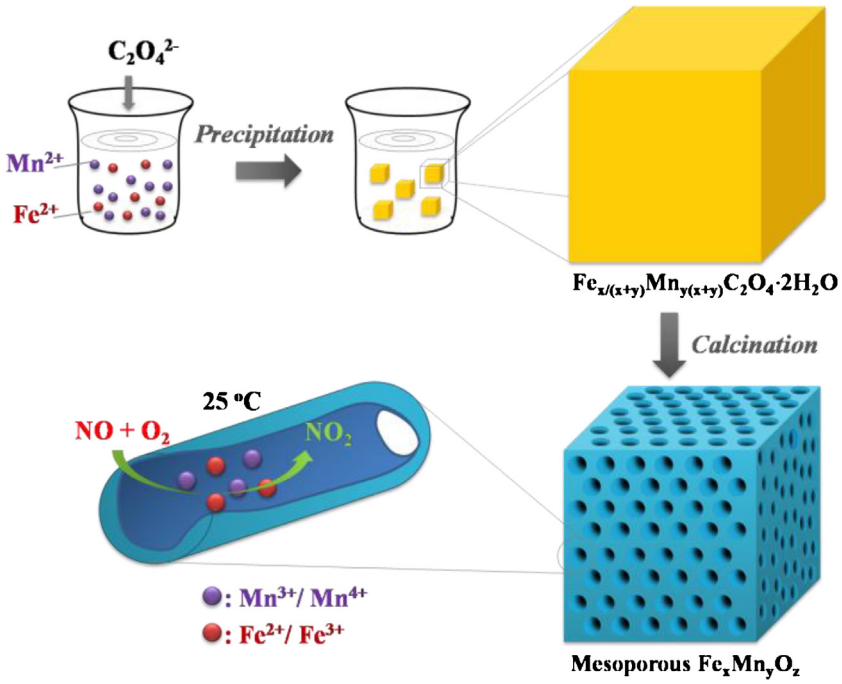

Fig. 11. Schematic diagram of the material synthesis process and application in efficient catalytic oxidation of NO at room temperature.

3.4. Summary of the design, synthesis and application of mesoporous Fe–Mn binary oxide

The design, synthesis and NO removal application of mesoporous Fe–Mn binary oxide are summarized and illustrated in Fig. 11. That is, a single-phase precursor of Fe–Mn binary oxalate can be precipitated from a Fe^{2+}–Mn^{2+} solution mixed with oxalic acid (as detailed in the Section 3.1). Controlled calcination on the precursor can decompose the $C_2O_4^{2-}$ anions and structural water into gaseous CO_2 and H_2O, leaving behind single-phase Fe–Mn binary oxide with well-structured mesoporosity and a high surface area (as detailed in the Section 3.2). A synergetic effect between Mn^{n+} and Fe^{n+} might catalyze the conversion of NO and O_2 into NO_2 at room temperature, which can be subsequently adsorbed/absorbed on the Fe–Mn binary oxide, ensuring a high efficiency of NO removal at room temperature (as detailed in the Section 3.3).

4. Conclusions

Mesoporous Fe–Mn binary oxide has been synthesized by a template-free controlled thermal decomposition approach from single-phase Fe–Mn binary oxalate, which was prepared by precipitation from a Fe^{2+}–Mn^{2+} solution mixed with oxalic acid. The 300 °C calcined Fe–Mn binary oxides were found to be amorphous single-phase material with homogeneous worm-like mesopores of 4–5 nm in diameters and high surface areas above 200 m^2/g. Increased Fe/Mn ratios from 1/8 to 1/2 resulted in increased specific surface areas and decreased pore sizes.

The amorphous and mesoporous Fe–Mn binary oxide of Fe/Mn ratio = 1/4 calcined at 300 °C demonstrated the best NO removal performance at room temperature among all prepared materials: 100% removal of 10 ppm NO for 4 h at a space velocity of 40,000 h^{-1}, and could be thermally regenerated for reuse. NO was suggested to be catalytically oxidized to NO_2 and then adsorbed/absorbed on/in Fe–Mn oxide by forming nitrites/nitrates. A synergetic effect between Mn^{n+} and Fe^{n+} was proposed to be responsible for the activation of NO and O_2 and their catalytic conversion into NO_2. The as-synthesized mesoporous Fe–Mn binary oxide had potential for the NO_x removal at room temperature in road tunnels and indoor parks.

Acknowledgments

The authors gratefully acknowledge the support of this research by National Basic Research Program of China (973 Program, 2013CB933200), Key Program for Science and Technology Commission of Shanghai (11JC1413400), China National Funds for Distinguished Young Scientists (51225202), National Natural Science Foundation of China (21177137, 51202278), Natural Science Foundation of Shanghai (12ZR1435200), State Key Laboratory of Heavy Oil Processing (2012-1-04).

Appendix A. Supplementary data

Supplementary data associated with this article can be found, in the online version, at http://dx.doi.org/10.1016/j.apcatb.2013.03.030.

References

[1] M. Almeida-Silva, N. Canha, M.C. Freitas, H.M. Dung, I. Dionisio, Applied Radiation and Isotopes 69 (2011) 1586–1591.
[2] G.L. Guerrini, Construction and Building Materials 27 (2012) 165–175.
[3] T. Maggos, J.G. Bartzis, M. Liakou, C. Gobin, Journal of Hazardous Materials 146 (2007) 668–673.
[4] G. Busca, L. Lietti, G. Ramis, F. Berti, Applied Catalysis B: Environmental 18 (1998) 1–36.
[5] N. Takahashi, K. Yamazaki, H. Sobukawa, H. Shinjoh, Applied Catalysis B: Environmental 70 (2007) 198–204.
[6] Z.R. Ismagilov, M.A. Kerzhentsev, Catalysis Reviews: Science and Engineering 32 (1990) 51–103.
[7] S. Hodjati, C. Petit, V. Pitchon, A. Kiennemann, Applied Catalysis B: Environmental 27 (2000) 117–126.
[8] O. Monticelli, R. Loenders, P.A. Jacobs, J.A. Martens, Applied Catalysis B: Environmental 21 (1999) 215–220.
[9] S. Adapa, V. Gaur, N. Verma, Chemical Engineering Journal 116 (2006) 25–37.
[10] I. Mochida, Y. Kawabuchi, S. Kawano, Y. Matsumura, M. Yoshikawa, Fuel 76 (1997) 543–548.
[11] P. Nikolov, M. Khristova, D. Mehandjiev, Colloids and Surfaces A 295 (2007) 239–245.

[12] H.Y. Liu, Z.K. Zhang, Y.Y. Xu, Y.F. Chen, X. Li, Chinese Journal of Catalysis 31 (2010) 1233–1241.
[13] M. Iwamoto, A.M. Hernandez, T. Zengyo, Chemical Communications (1997) 37–38.
[14] H.Y. Huang, R.T. Yang, Langmuir 17 (2001) 4997–5003.
[15] J.L. Shi, Chemical Reviews 113 (2013) 2139–2181.
[16] Y. Wan, D.Y. Zhao, Chemical Reviews 107 (2007) 2821–2860.
[17] T. Sen, A. Sebastianelli, I.J. Bruce, Journal of the American Chemical Society 128 (2006) 7130–7131.
[18] M. Khairy, S.A. El-Safty, M. Ismael, H. Kawarada, Applied Catalysis B: Environmental 127 (2012) 1–10.
[19] A.L. Kustov, T.W. Hansen, M. Kustova, C.H. Christensen, Applied Catalysis B: Environmental 76 (2007) 311–319.
[20] Z. Gao, F.M. Cui, S.Z. Zeng, L.M. Guo, J.L. Shi, Microporous and Mesoporous Materials 132 (2010) 188–195.
[21] Y. Hasegawa, K. Fukumoto, T. Ishima, H. Yamamoto, M. Sano, T. Miyake, Applied Catalysis B: Environmental 89 (2009) 420–424.
[22] J.N. Kondo, K. Domen, Chemistry of Materials 20 (2008) 835–847.
[23] B. Puertolas, B. Solsona, S. Agouram, R. Murillo, A.M. Mastral, A. Aranda, S.H. Taylor, T. Garcia, Applied Catalysis B: Environmental 93 (2010) 395–405.
[24] D.N. Srivastava, N. Perkas, A. Gedanken, I. Felner, Journal of Physical Chemistry B 106 (2002) 1878–1883.
[25] Y.X. Rao, J.J. Kang, M. Trudeau, D.M. Antonelli, Journal of Catalysis 266 (2009) 1–8.
[26] H.R. Chen, X.P. Dong, J.L. Shi, J.J. Zhao, Z.L. Hua, J.H. Gao, M.L. Ruan, D.S. Yan, Journal of Materials Chemistry 17 (2007) 855–860.
[27] Y. Ren, Z. Ma, P.G. Bruce, Chemical Society Reviews 41 (2012) 4909–4927.
[28] X.Z. Cui, J. Zhou, Z.Q. Ye, H.R. Chen, L. Li, M.L. Ruan, J.L. Shi, Journal of Catalysis 270 (2010) 310–317.
[29] C.T. Kresge, M.E. Leonowicz, W.J. Roth, J.C. Vartuli, J.S. Beck, Nature 359 (1992) 710–712.
[30] X.Z. Cui, X.X. Zhou, H.R. Chen, Z.L. Hua, H.X. Wu, Q.J. He, L.X. Zhang, J.L. Shi, International Journal of Hydrogen Energy 36 (2011) 10513–10521.
[31] C.C. Yu, L.X. Zhang, J.L. Shi, J.J. Zhao, J.H. Gao, D.S. Yan, Advanced Functional Materials 18 (2008) 1544–1554.
[32] C.C. Yu, X.P. Dong, L.M. Guo, J.T. Li, F. Qin, L.X. Zhang, J.L. Shi, D.S. Yan, Journal of Physical Chemistry C 112 (2008) 13378–13382.
[33] G.S. Qi, R.T. Yang, Journal of Physical Chemistry B 108 (2004) 15738–15747.
[34] Z.H. Chen, F.R. Wang, H. Li, Q. Yang, L.F. Wang, X.H. Li, Industrial and Engineering Chemistry Research 51 (2012) 202–212.
[35] J.R. Scheffe, A. Frances, D.M. King, X.H. Liang, B.A. Branch, A.S. Cavanagh, S.M. George, A.W. Weimer, Thin Solid Films 517 (2009) 1874–1879.
[36] S. Tiwari, R. Prakash, R.J. Choudhary, D.M. Phase, Journal of Physics D: Applied Physics 40 (2007) 4943–4947.